Cement and Concrete Research 143 (2021) 106376

Contents lists available at ScienceDirect

Cement and Concrete Research

journal homepage: www.elsevier.com/locate/cemconres

Coordination environment of Si in calcium silicate hydrates, silicate minerals, and blast furnace slags: A XANES database

Jiaqi Li [a,*], Wenxin Zhang [a], Krassimir Garbev [b], Paulo J.M. Monteiro [a]

[a] Department of Civil and Environmental Engineering, University of California, Berkeley, CA 94720, United States
[b] Institute for Technical Chemistry, Karlsruhe Institute of Technology, 76021 Karlsruhe, Germany

ARTICLE INFO

Keywords:
XANES
X-ray absorption spectra
C-S-H
Tobermorite
Silicate polymerization

ABSTRACT

Understanding the silicate polymerization of calcium silicate hydrate (C-S-H) gel and its crystalline polymorphs is important in cement science. NMR can determine Si environments, but the measurement can be time-consuming and provides no spatial information. X-ray absorption near-edge structure (XANES) spectroscopy is a fast tool for probing Si coordination, possibly with spatial information. However, there lacks an understanding of Si K-edge XANES spectra of cement-related silicate phases. Here, a Si K-edge XANES spectral database of nanocrystalline C-S-H, C-S-H minerals, blast-furnace slags, and metakaolin is provided. Si K-edge of C-S-H minerals shifts to higher energies with higher polymerized Si and lower Ca—Si connectivity in the Si second nearest neighbor shell. Si K-edge energy shows weak correlations with Ca/Si ratio, average Si—O bond length, and SiO_4 distortion due to the structural complexity of silicates. The substitution of Al for Si shifts the Si K-edge of tobermorite and slags to higher energies.

1. Introduction

Silicon is an important element in the fields of binders and concrete. The commonly used binders – Portland cement, alkali-activated materials, belite-ye'elimite-ferrite cement, and carbonated silicate – are Si-rich [1–3]. These Si-rich binder systems are highly complex. Blast-furnace slags and calcined clay from various origins have different compositions. The silicate binding phases of these systems under ambient conditions are X-ray amorphous (e.g., calcium silicate hydrate (C-S-H) gel, sodium aluminosilicate hydrate gel, and silica gel) [4–7] or (nano) crystalline (e.g., sodium/potassium incorporated calcium aluminosilicate hydrate I and strätlingite) [8–12]. Under autoclave or geological conditions (e.g., oil wells), crystalline C-S-H minerals (e.g., *Z*-phase, tobermorite, xonotlite, hillebrandite, trabzonite, and killalaite) form in hardened cementing materials [13–15]. The alkali-silica reaction products around concrete aggregates are amorphous or crystalline silicates [16–18].

The phase and chemical compositions of hardened cementitious systems and concrete are highly heterogeneous. Understanding the local chemistry of Si-bearing materials is important as the Si environment influences the intrinsic mechanical properties of silicates and durability of cementitious systems [3,19–22]. The coordination environment of Si is very complex. Although Si in most of the Si-containing phases is four-fold coordinated [23], Si in thaumasite is six-fold coordinated [24] similarly as in the high pressure SiO_2 polymorph stishovite [25]. Five-fold coordinated Si has also been reported in $CaSi_2O_5$ under high pressure conditions [26]. The wide variety of four-fold coordinated Si in silicates is categorized into $Q^n(m\text{Al})$, which designates a SiO_4 tetrahedron connected to (n-*m*) SiO_4 tetrahedra and *m* AlO_4 tetrahedra [5] where m and n vary from 0 to 4. Many conventional characterization techniques, e.g., X-ray diffraction, selected area electron diffraction, and Raman spectroscopy, typically only yield useful data of (nano)crystalline C-S-H, but not on C-S-H gel formed during the cement hydration [27–29]. For example, Raman spectroscopy shows limitations in the study of C-S-H gel as its Q^n (*m*Al) related resonance is highly diffuse [30,31]. Solid-state nuclear magnetic resonance (NMR) spectroscopy provides valuable qualitative or quantitative information of Q^n [32–35]. However, ^{29}Si NMR only provides bulk chemical information and the measurement typically takes tens of hours, which makes in situ studies challenging. Recent advances in NMR using ^{29}Si enriched samples [36] and dynamic nuclear polarization [37] allow shorter data collection periods and make in situ ^{29}Si NMR studies of cementitious systems possible.

X-ray absorption near-edge structure (XANES) spectroscopy allows

* Corresponding author at: 115 Davis Hall, University of California, Berkeley, Berkeley, CA 94720, United States.
E-mail address: Jiaqi.li@berkeley.edu (J. Li).

https://doi.org/10.1016/j.cemconres.2021.106376
Received 30 October 2020; Received in revised form 29 December 2020; Accepted 13 January 2021

in situ studies of changes in the coordination environment of elements [38,39]. XANES spectromicroscopy is a powerful tool for 2D and 3D-mapping of phases and determining the coordination chemistry of both amorphous and crystalline phases [40–43]. Recent advances in X-ray spectromicroscopy, e.g., scanning transmission X-ray microscopy (STXM), allow experiments with spatial resolution down to 8 nm [44], which is much finer than that of advanced Raman spectromicroscopy (e.g., Raman micro-spectroscopy) and scanning X-ray micro diffraction [45–47]. Although 8-nm spatial resolution is lower than that of electron energy loss spectroscopy (EELS), XANES allows the study of thicker samples than EELS (5 μm vs. 10's nm) [48]. Moreover, the sample preparation for XANES studies is much easier and induces fewer artifacts.

XANES has been applied to cement science (e.g., calcium silicate hydration) [49,50]. A correlation between silicate polymerization of C-S-H gel and Si K-edge of XANES spectra has been found [4,22,51]. Yet, the Si K-edge XANES spectra of many other phases in cementitious systems remain unknown. A more comprehensive database of Si K-edge XANES spectra of construction materials-relevant Si phases is needed for future studies of complex cementitious systems. There is a lack of a deep understanding of the X-ray absorption features of silicate phases in complex heterogeneous binder systems (e.g., poorly ordered C-S-Hs in Portland cement hydration and alkali-activated slag). Understanding the relationship between the absorption features in XANES spectra and local Si environments (e.g., Ca/Si ratio, Ca—Si connectivity, and Q^n coordination) will advance the study of the local structural changes of binder hydration/activation over time using the STXM with the spatial resolution down to 8 nm [52] [44].

This experimental study presents a XANES database at the Si K-edge of Si-rich phases relevant to construction materials. The Si phases include C-S-H minerals (*Z*-phase, killalaite, xonotlite, hillebrandite, trabzonite, suolunite, and afwillite), nanocrystalline C-S-H, tobermorite with various Al content, amorphous (calcium) aluminosilicate, stratlingite, thaumasite, metakaolin, blast-furnace slag with various compositions, and other Si rich phases, such as scawtite. The extensive database of XANES spectral features at Si K-edge can be used to characterize complex heterogeneous binder systems, and to locally determine the phase and composition change of hydrating systems in situ using STXM.

2. Materials and method

2.1. Materials

Natural samples of afwillite, scawtite, wollastonite, and 14 Å tobermorite (Plombièrite) were obtained from Crestmore, California, United States. Natural samples of xonotlite and poldervaartite were obtained from N'Chwaning, South Africa. Natural suolunite was obtained from Lac D'Amiante, Québec, Canada. Natural foshagite and thaumasite were obtained from the Berkeley Mineral collections. Natural okenite was obtained from Puna District, India. Natural gyrolite was obtained from Malad, India.

Stratlingite was synthesized by starting from a stoichiometric mix of CaO, sodium silicate, and $NaAlO_2$ in deionized water at 23 °C. All chemicals were separately dissolved in water at 25 °C. The $NaAlO_2$ solution was added to the portlandite solution, followed by the addition of silicate solution. The resulting suspension was stirred for 60 days at 23 °C prior to filtration.

All synthetic C-S-H mineral samples were hydrothermally synthesized in Teflon lined autoclaves at temperatures between 70 and 240 °C. All sample preparations of synthetic minerals were performed under N_2 to avoid carbonation.

11 Å Al-free and Al double-chain tobermorite (cross-linked) were synthesized in two step procedure. C-S-H slurry with a Ca/Si molar ratio of 5/6 (Al-free) and C-A-S-H slurries with Ca/(Al + Si) ratio of 5/6 and Al/(Al + Si) in molar ratios of 1/64, 1/32, and 1/12 were obtained by mixing of CaO, amorphous silica (Aerosil 200), $Al(OH)_3$ and double distilled water (w/s = 20). The mixtures were mechanochemically treated in an agate ball mill for 32 h. The resultant slurries were autoclaved at 170 °C for 22 h followed by further 2 h at 180 °C. The solids were filtered, rinsed, and dried at 60 °C. More details can be found in [21,53].

14 Å tobermorite and jennite were synthesized by curing at 70 °C for 12 months from mechanochemically prepared C-S-H with Ca/Si ratios of 5/6 and 3/2, respectively. 11 Å single-chain tobermorite (non-cross-linked) was synthesized by dehydrating a synthetic 14 Å tobermorite at 100 °C for 3 h. Metajennite was prepared by dehydrating the synthetic jennite at 150 °C for 12 h. This dehydration protocol was selected because further dehydration of jennite at a higher temperature, e.g., 350 °C, would destabilize the Ca-OH group in metajennite, forming an amorphous phase [54].

Z-phase was obtained by autoclaving mechanochemically treated slurry with C/S = 0.56 at 190 °C for 16 h. Hillebrandite was prepared by hydrothermal treatment of a C-S-H (I) and $Ca(OH)_2$ mixture with C/S = 2.0 at 200 °C for 168 h. Trabzonite and killalaite were prepared from Ca$(OH)_2$ (p.a.), H_2O and SiO_2 (Aerosil 200), in C/S of 4/3 and 1.75, respectively, at 240 °C (3 weeks) under hydrothermal conditions.

Nanocrystalline C-S-H was synthesized from dilute hydration of triclinic tricalcium silicate at w/s of 900 at room temperature. The bulk Ca/Si molar ratio of the nanocrystalline C-S-H is 1.0.

Amorphous content ($Al_2Si_2O_7$) of metakaolin (Metamax, BASF) used in this study is over 97 wt% with ~1 wt% muscovite and ~ 1 wt% anatase. Ground granulated blast-furnace slag (GGBFS) from different origins were used for XANES measurement. The chemical compositions of the GGBFS, synthetic slag, and metakaolin are listed in Table 1.

The purity of all samples was 97+ wt%, mostly validated by X-ray diffraction. The purity of the slags [55,56], xonotlite [57], and tobermorites [21] was confirmed in previous studies.

2.2. X-ray absorption near-edge structure spectroscopy

The Si K-edge XANES spectral measurements were performed at the PHOENIX beamline (station II) at the Swiss Light Source in Paul Scherrer Institute, Switzerland. The data were obtained using a fluorescence-yield mode with a beam size of 500 μm × 500 μm at room temperature. Fine powder samples were lightly pressed onto indium foils and then attached to a copper plate. The plate was mounted on a sample stage in a vacuum chamber. The spectra were recorded at an energy step of 0.2 eV for 1 s for each data point. Each Si K-edge peak position in this study was taken by averaging the energy position of seven data points with the highest intensities. This approach has been commonly used in XANES spectral analyses.

3. Results and discussion

3.1. Si K-edge and Ca/Si molar ratio

Si K-edge XANES spectra of the minerals are shown in an increasing Ca/Si molar ratio in Fig. 1A. In general, five features (A, B, C, D, and E) are present in the spectra. The pre-edge shoulder A at ~1837 eV is ascribed to the dipole-forbidden transition of Si 1s electron to anti-bonding 3s-like states. Thus, left-shoulder A is extremely weak and could only be observed here in wollastonite, trabzonite, and thaumasite (indicated by the blue arrows). The major peak B (Si K-edge peak, ~1840 eV) is attributed to the transition of Si 1s electrons to anti-bonding 3p-like states, which is dipole allowed by selection rules and thus of high intensity [58]. And the right-shoulder C is frequently observed at ~3 eV above the edge, attributable to the multiple scattering effect from more distant atomic shells [58,59]. The post edge minor peak D (varying between 1845 and 1855 eV) and the very diffuse peak E (~1860 eV) are assigned to the multiple scattering effect from more distant atomic shells [59,60] and the electron transitions (e, t_2) from Si

Table 1
Oxide compositions of metakaolin, GGBFS, and synthetic slag.

Oxide composition	Metakaolin	CAN [55]	AU [55]	US	CN	UAE	EUA7 [56]	EUA14 [56]	EUA17 [56]
CaO	0.04	33.92	42.33	42.57	41.59	41	39.1	36	35
SiO_2	51.75	37.04	32.25	32.48	30.86	36.6	41.6	38.2	37.2
Al_2O_3	45.01	8.95	13.29	12.77	14.36	14.2	7	14.1	16.7
MgO		14.32	5.21	6.79	10.86	4.03	7.2	6.6	6.4
SO_3	0.07	0.74	2.86	2.84	1.66	1.98	1.3	1.2	1
Fe_2O_3	0.41	0.4	0.6	0.86		0.79	1.3	1.4	1.4
TiO_2	1.41	0.38	0.49	0.69	0.66	0.57	0.3	0.3	0.2
MnO		0.99	0.19	0.36		0.18	1.1	1	1
K_2O	0.12	0.54	0.33	0.34		0.39	0.6	0.6	0.5
Na_2O		0.23		0.26			0.5	0.5	0.5
P_2O_5	0.1	0.05	0.03	0.01					
Others	1.09	2.08	2.42	–	–	0.26	–	–	–

Note: CAN, AU, US, CN, EU designate slags from Canada, Australia, United States, China, and Europe, respectively. A7, A14, and A17 designate Al_2O_3 mass fraction of synthetic slags in percentage.

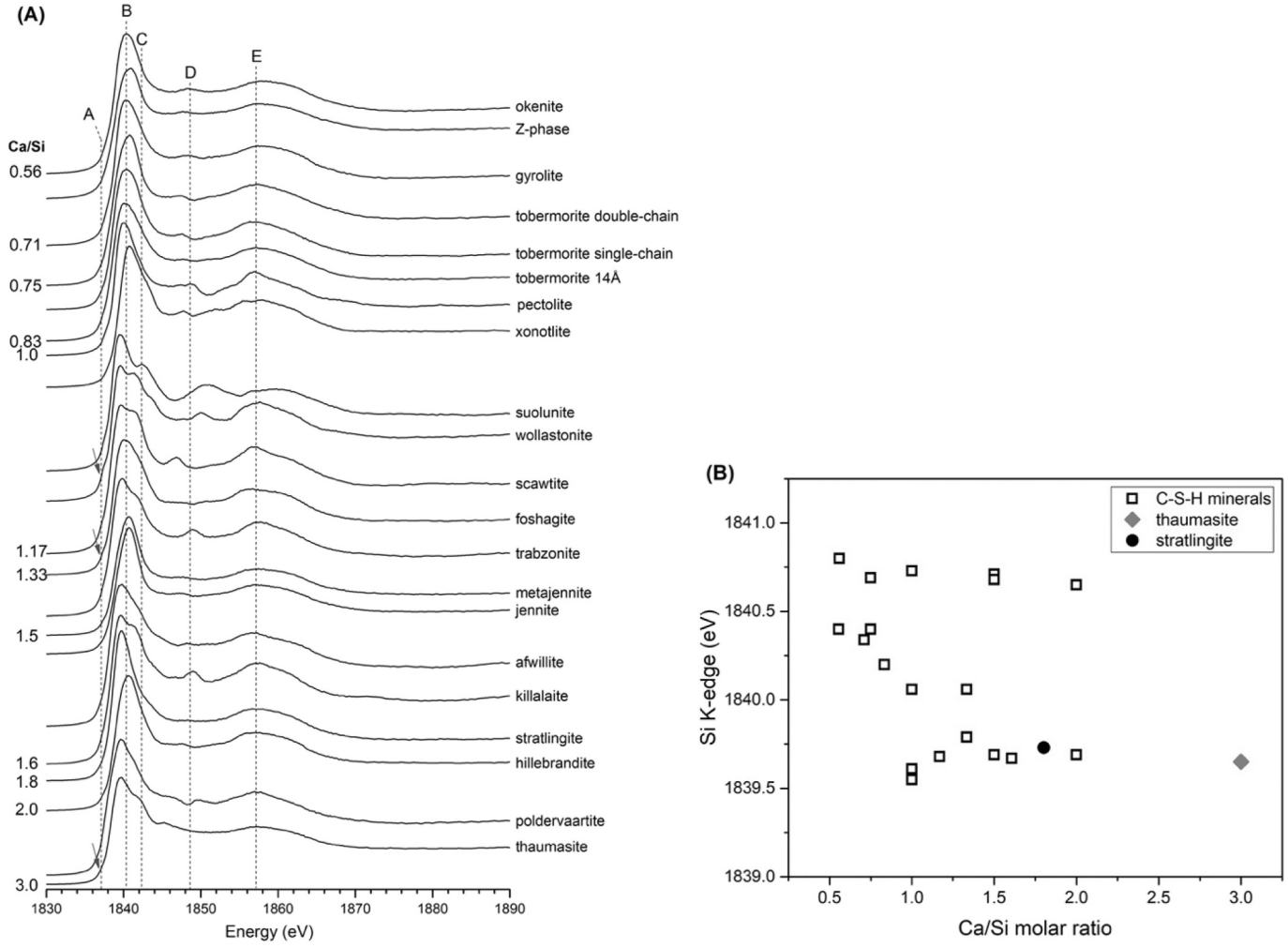

Fig. 1. (A) Si K-edge XANES spectra of the minerals, in the sequence of Ca/Si molar ratio. Thaumasite with six-fold coordinated Si does not present distinguishable features in the Si K-edge XANES spectrum compared to the rest minerals with four-fold coordinated Si. (B) The relationship between the Si K-edge and the Ca/Si molar ratio of the minerals in Figure A. Note that Ca/Si ratio is substituted with (Ca + Na)/Si in pectolite, (Ca + Mn)/Si in poldervaartite, and (Ca + Na)/(Si + Al) in gyrolite.

1s to 3d orbitals [58], respectively.

There are great spectral differences among the minerals in their post-edge features (i.e., peaks C, D, and E) due to complex multiple scattering and possible splitting of 3d orbitals. The complex post-edge features preclude drawing explicit correlations between their positions and the local Si bonding environment. Nevertheless, they can still provide signature information, e.g., when needed to differentiate phases with similar medium-range (10–20 Å) structures from non-similar counterparts (see later discussions on nanocrystalline C-S-H and slags). The Si K-edge position is the most distinguishable feature and will be extensively discussed in this study. At the examined Ca/Si ratio of 0.56–3.0 of the minerals, the Si K-edge fluctuates between 1839.5 and 1840.8 eV and

does not possess any noticeable correlation with the Ca/Si molar ratio (Fig. 1B).

3.2. Si K-edge and the connectivity of Si atoms

The Si K-edge energy is influenced by neighbor shells of atoms. In the presently studied C-S-H minerals, the first nearest neighbor shell to a Si atom is predominated by oxygen. The second nearest neighbor shell is mainly shared by Si and Ca, and the presence of no more than one Si-OH per Si atom is also common (e.g., in killalaite [61], suolunite [62], 11 Å tobermorite [63], and poldervaartite [64]). As the only exception, pectolite contains Na in addition to Si, Ca, and H in the second nearest neighbor shell of Si [65]. The center Si atom and the second-shell atoms are both bonded to the neighbor oxygen, forming Si—O—Si and Si—O—Ca. In analogous to Q^n that conventionally defines the Si (second shell)-Si (center) connectivity, we introduce the concept of Ca—Si connectivity, which is equal to the number of Ca atoms in the second nearest neighbor shell of the center Si atom. The Q^n and Ca—Si connectivity of silicate minerals are extracted from existing literature (afwillite [66], foshagite [67], gyrolite [68], hillebrandite [69], jennite [54], killalaite [61], okenite [70], pectolite [65], poldervaartite [64], scawtite [71], stratlingite [72], suolunite [62], thaumasite [73], tobermorite (single-chain, double-chain, and 14-Å) [74] [75] [76], trabzonite [77], wollastonite [65], xonotlite [78], and *Z*-phase [79]). Among all Si atoms in the minerals, Q^n, ranges from Q^0 to Q^3 (Fig. 2A), with a majority of Si being Q^2 or Q^3. On the other hand, the values of Ca—Si connectivity traverse every whole number between zero and eight in these minerals (Fig. 2B).

Note that in the following discussion, the minerals are divided into the C-S-H minerals and two separate minerals – stratlingite and thaumasite – because the latter two possess features distinct to all other minerals in the present study. In strätlingite, the silicate tetrahedral double-layer is sandwiched by the Ca—O layers in the absence of covalent or ionic bonding in between (Fig. 3A). Thus, it totally lacks Ca—Si connectivity, which does not happen in any other presently examined minerals. Thaumasite contains only six-fold coordinated $Si(OH)_6$ (Fig. 3B) while all other minerals contain four-fold coordinated Si only. Therefore, the term – C-S-H related minerals – in all following discussions excludes stratlingite and thaumasite.

A clear shift of the Si K-edge to higher energies with an increasing average Q^n is observed in C-S-H minerals (Fig. 4A), accompanied by irregular shifts of the post-edge minor peaks D and insignificant shifts of the diffuse hump E. At lower Q^n values, below two, the Si K-edge is at ~1839.6–1839.8 eV; at the higher Q^n value above two, the Si K-edge occurs in another non-overlapping narrow range of ~1840.4–1840.8 eV (Fig. 4B). Only the Si K-edge of Q^2 exhibits a wide range (1839.6–1840.7 eV). The intrinsic mechanism behind this shift of Si K-edge is the progressively increasing effective charge on Si progressively with increasing Q^n [58,80].

Note that the two Q^0 C-S-H minerals, afwillite and poldervaartite, possess comparable Si K-edge as the Q^1 counterparts. This fact is explained that in the two minerals, the second-shell proton of the central Si participate in the formation of chain-like hydrogen bonds. The second-shell hydrogen, with electronegativity slightly higher than Si, increases the effective charge of Si whose K-edge thus shifts to higher energy. Therefore, the Q^0 minerals with Si-OH and strong hydrogen bonding can possess comparable Si K-edge as the higher Q^n phases. In general, the characteristic distribution of the Si K-edge as a function of Q^n can perform as a reliable empirical reference for estimating the average Q^n of nanocrystalline C-S-H samples. The shift of Si K-edge toward higher energy with increased Q^n was also confirmed in [58] where the edge increased by 1.3 eV from forsterite (Mg_2SiO_4, Q^0) to α-quartz (SiO_2, Q^4). Furthermore, the present observation is consistent with the findings from the studies of similar phases using X-ray photoelectron spectroscopy (XPS). The XPS studies showed a clear increase of the Si 2p binding energy (BE) with increasing Q^n [79,80], explained by decreased residual negative charge of the silicate and decreased shielding effect on the Si atom.

Beside the second-shell Si atoms, the second-shell metal cations (predominantly Ca in the present study) also affect the Si K-edge energy. When plotted in the sequence of increasing Ca—Si connectivity, the Si K-edge XANES spectra demonstrate a gradual shift of the K-edge to slightly lower energy (Fig. 5A). In addition, the shoulder peak C is generally absent for Ca—Si connectivity below ~4.0–5.0. Above this value, however, the shoulder peak C is often easily recognizable and yet it does not present an obvious trend between its position and the Ca—Si connectivity. The shift of the minor peak D is also irregular, and the variation in the diffuse hump E is negligible. A moderate negative correlation exists between Si K-edge and Ca—Si connectivity of the C-S-H minerals, with $R^2 = 0.48$ (Fig. 5B): the Si K-edge decreases by ~1.1 eV from ~1840.8 eV at low Ca—Si connectivity of 2.5 to ~1839.7 eV at high Ca—Si connectivity of 7–8. The trend between the shift of Si K-edge and Ca—Si connectivity can be explained by noting that the presence of more second-shell Ca reduces the effective charge on the Si atom and lowers the Si K-edge energy. The outlier data point associated to strätlingite can be explained by the three Si-OH bonding per Si atom, in contrast the average number of Si-OH bond per Si atom in the C-S-H minerals is no more than one. In strätlingite, the second-shell proton

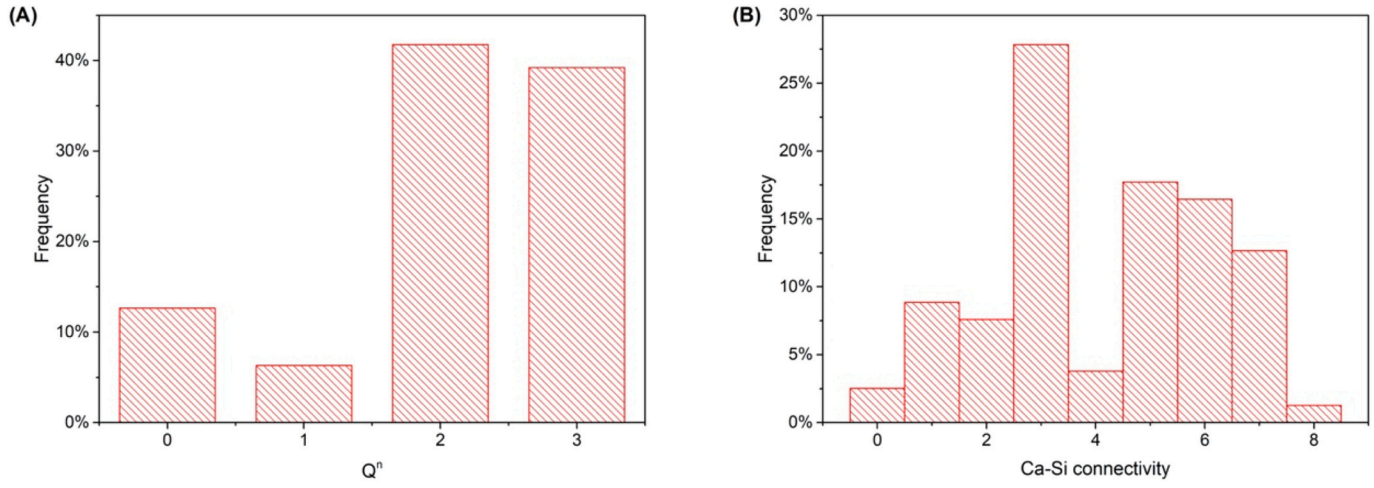

Fig. 2. Statistics of (A) Q^n and (B) Ca—Si connectivity of each Si atom in afwillite [66], foshagite [67], gyrolite [68], hillebrandite [69], jennite [54], killalaite [61], okenite [70], pectolite [65], poldervaartite [64], scawtite [71], stratlingite [72], suolunite [62], thaumasite [73], tobermorite (single-chain, double-chain, and 14-Å) [74] [75] [76], trabzonite [77], wollastonite [65], xonotlite [78], and *Z*-phase [79]. The number of different Si atoms is 79.

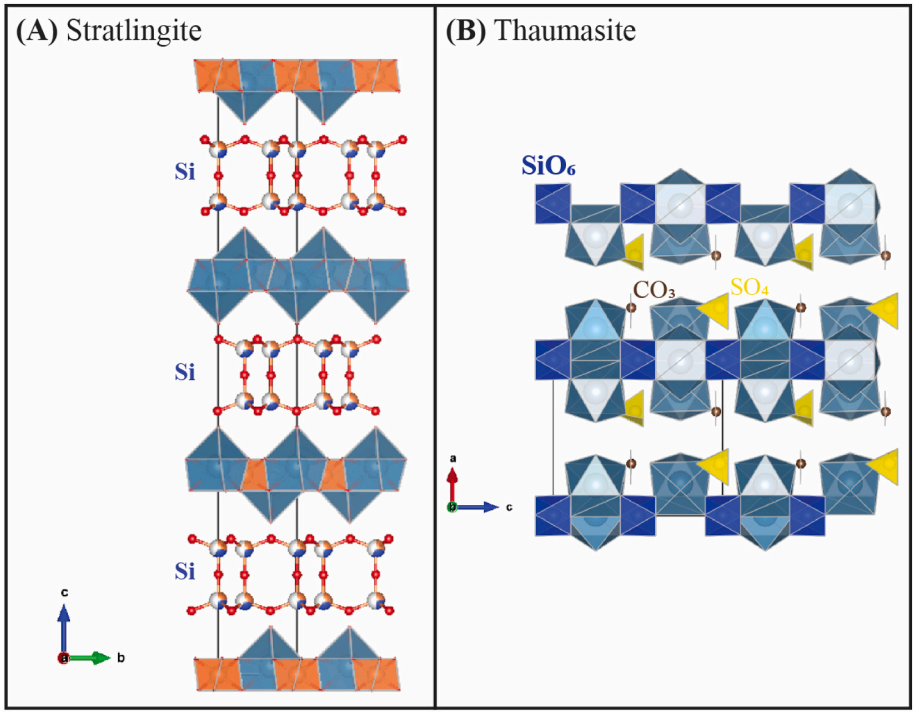

Fig. 3. The crystal structure of (A) stratlingite featuring no Ca—Si and (B) thaumasite featured by SiO_6 units. The outlined grey box indicates the unit cell of the crystal structure. Ca polyhedron is illustrated in green, silicates in blue, Al polyhedron in orange, SO_4 in yellow, and CO_3 in brown; oxygen atoms at the corners of every polyhedron are omitted for clarity. The Si-containing layers in stratlingite consist of sites shared by Si and Al with partial occupancy — the resulted average connectivity of the silicate is Q^2. (For interpretation of the references to color in this figure legend, the reader is referred to the web version of this article.)

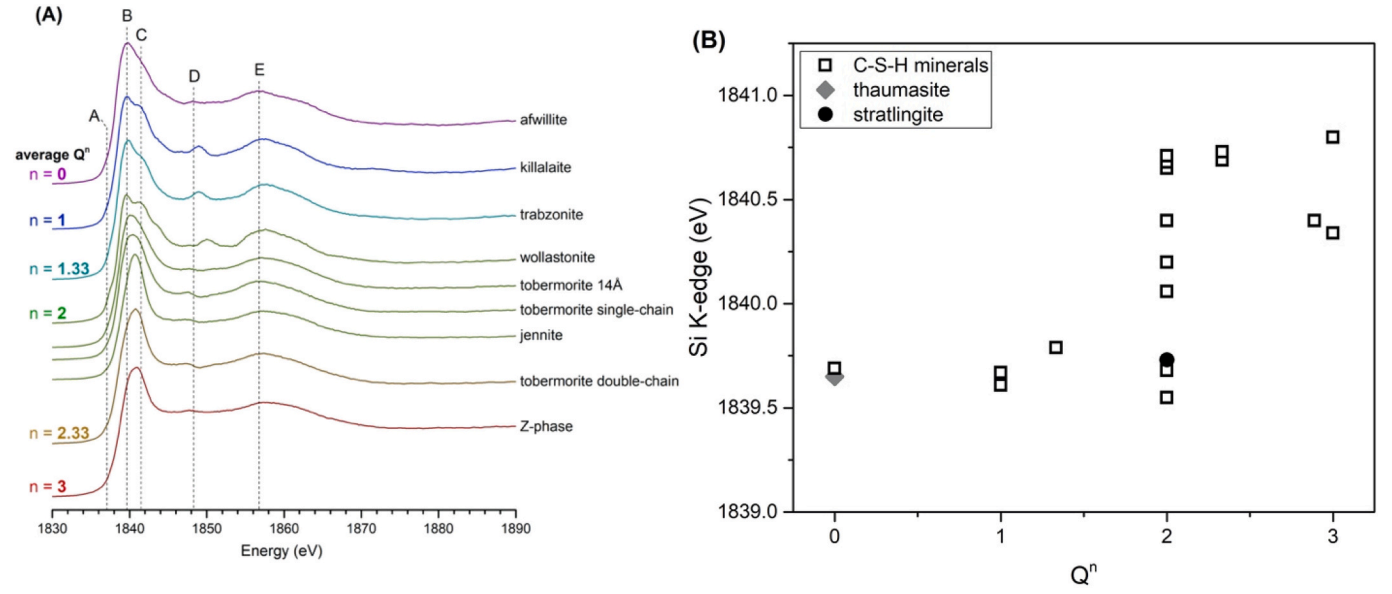

Fig. 4. (A) Si K-edge XANES spectra of the selected minerals in the sequence of average Q^n. (B) The relationship between Q^n and Si K-edge of all the studied minerals.

pulls the first-shell oxygen away from the Si atom and weakens the Si—O bond, and thus, the Si K-edge shifts to a lower energy.

The weak linear correlation ($R^2 = 0.48$) between the Ca—Si connectivity and Si K-edge indicates that other factors are relevant. Thus far, the positive correlation between Q^n and Si K-edge has been observed for the C-S-H minerals. Indeed, Q^n and the Ca—Si connectivity themselves are intrinsically correlated since the stacking of silicate tetrahedra and CaO_x polyhedra follows specific patterns in the C-S-H related minerals.

Representative structures of the C-S-H minerals are demonstrated in Fig. 6 in the increasing value of Q^n. At smaller Q^n values, silicate monomers Q^0, (e.g., afwillite in Fig. 6A), dimers Q^1, (e.g., suolunite in Fig. 3B), and trimers Q^1 with Q^2 (e.g., trabzonite in Fig. 6C) decorates the Ca—O layers. At intermediate Q^n values around two, the silicate forms infinite chains in, e.g., foshagite, jennite, tobermorite (Fig. 6D), and wollastonite. At Q^n, as high as three, the silicate forms infinite 2D networks in, e.g., okenite and *Z*-phase (Fig. 6E). On the other hand, the values of Ca—Si connectivity traverse every whole number between zero and eight in these minerals. Among all possible values, the Ca—Si connectivity of three (most commonly achieved by silicates with a flat Ca—O layer on one side; e.g., gyrolite, Z-phase), five (silicates with a staggered Ca—O layer on one side; e.g., the bridging site silicate in tobermorite), six, and seven (silicates with Ca—O layers on both sides; trabzonite, wollastonite) are more common than the others.

The Ca/Si molar ratio of the minerals varies from 0.56 to 3.0, in moderately positive correlation with Ca—Si connectivity but weak

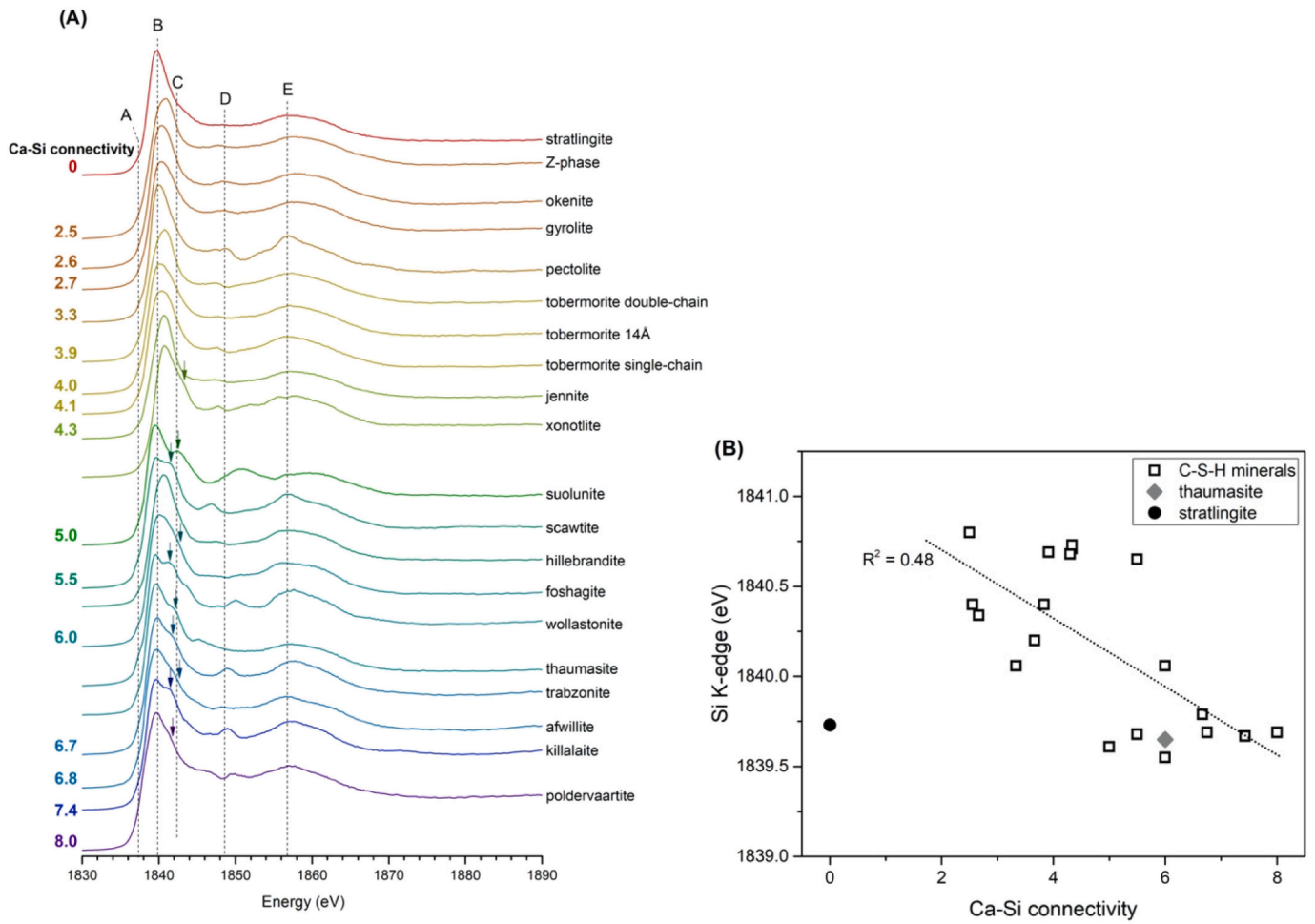

Fig. 5. (A) Si K-edge XANES spectra of the selected minerals in the sequence of average Ca—Si connectivity. Note that the actual Ca—Si connectivity of poldervaartite may vary between four and eight as the same site of Ca may be shared by Mn (<50%), but the M^{2+} (i.e., Ca^{2+} and Mn^{2+})-Si connectivity of poldervaartite is always eight. (B) The relationship between the Si K-edge and the average Ca—Si connectivity of all the studied minerals. Stratlingite is excluded from the regression.

correlation with Q^n (Fig. 7A). At the lower end of Ca/Si, each SiO_4 bonds to a roughly equal number (i.e., ~2–3) of Ca and Si. As Ca/Si increases to ~1.5, the SiO_4 could maximally bond with eight Ca while its connectivity with other SiO_4 does not considerably decrease. In general, the wider range of Ca—Si connectivity compared to Q^n is related to the greater length of Ca—O than Si—O bonds (i.e., ~2.5 Å compared to ~1.6 Å). Ca—Si connectivity and Q^n are in clear negative correlation (Fig. 7B), with $R^2 = 0.71$ for the C-S-H minerals. In addition, the average total connectivity (Ca—Si connectivity plus Q^n) in the C-S-H minerals varies in the range of 5.3–8.4, or 5.4–9.0 if Si-OH is additionally counted. However, there is no obvious correlation between the total connectivity and Si K-edge (Fig. S1 in Supplementary Information (SI)).

3.3. Si K-edge and SiO_4/SiO_6

The relationship between the first atomic shell and Si K-edge is worth discussing. Among 318 different Si—O bonds in the examined minerals, the average bond length is 1.629 Å with an overall standard deviation of 0.049 Å. ~90% falls within 1.58–1.69 Å (Fig. 8A). Two minerals are outliers in the Si—O bond length distribution: strätlingite with an average bond length of 1.738 Å and thaumasite 1.783 Å. The longer Si—O bond in strätlingite is explained by (a) the partial occupancy of and Al at the same site and (b) the presence of three long Si-OH per Si atom. Different from all other examined silicates (four-fold coordinated), Si in thaumasite forms SiO_6; and the six second-shell protons per Si atom also result in longer Si—O bond. Additionally, there exists a weak correlation between the average Si—O bond length and Q^n of the individual Si atoms (Fig. S2A in SI). A spectral comparison between thaumasite and stishovite (also with SiO_6) [59] is worth mentioning. Stishovite shows a peak B at 1849 eV, which is higher than that of thaumasite and quartz. Nevertheless, there are also such similarities as presence of the peaks A and C between both minerals. The long Si—O bonds, the low Q^n, and the protons explain the low Si K-edge energy of thaumasite. No obvious relationship is observed between the average Si—O bond length and the Ca—Si connectivity (Fig. S2B in SI). The distortion of individual SiO_4 or SiO_6 (i.e., the standard deviation of the Si—O bond lengths in individual $SiO_{4/6}$) is mostly (~80%) within 0.1–0.05 Å (Fig. 8B). The phase-average $SiO_{4/6}$ distortion is <0.06 Å, indicating a low distortion degree of the $SiO_{4/6}$ in all examined minerals. No noticeable relationship between the phase-average distortion of SiO_4/SiO_6 and Q^n or Ca—Si connectivity is observed (Fig. S3 in SI).

Although the C-S-H minerals present a wide variety in their second nearest neighbor shell, they are essentially similar in the first atomic shell. While Si K-edge is shown in a clear correlation with the connectivity to the second-shell Ca and Si, it presents no obvious relation to the first-shell O (Fig. 9A). This lack of correlation was also found in [58], attributed to complexity in the crystal structures. For similar reasons, no evident correlation between the Si K-edge and the distortion of single SiO_4/SiO_6 could be concluded (Fig. 9B). There exists no obvious trend in the Si K-edge as a function of the phase-average maximum or minimum Si—O bond length of each SiO_4 or SiO_6 in different phases (Fig. S4 in SI). However, the Si K-edge and average Si—O bond length correlation still

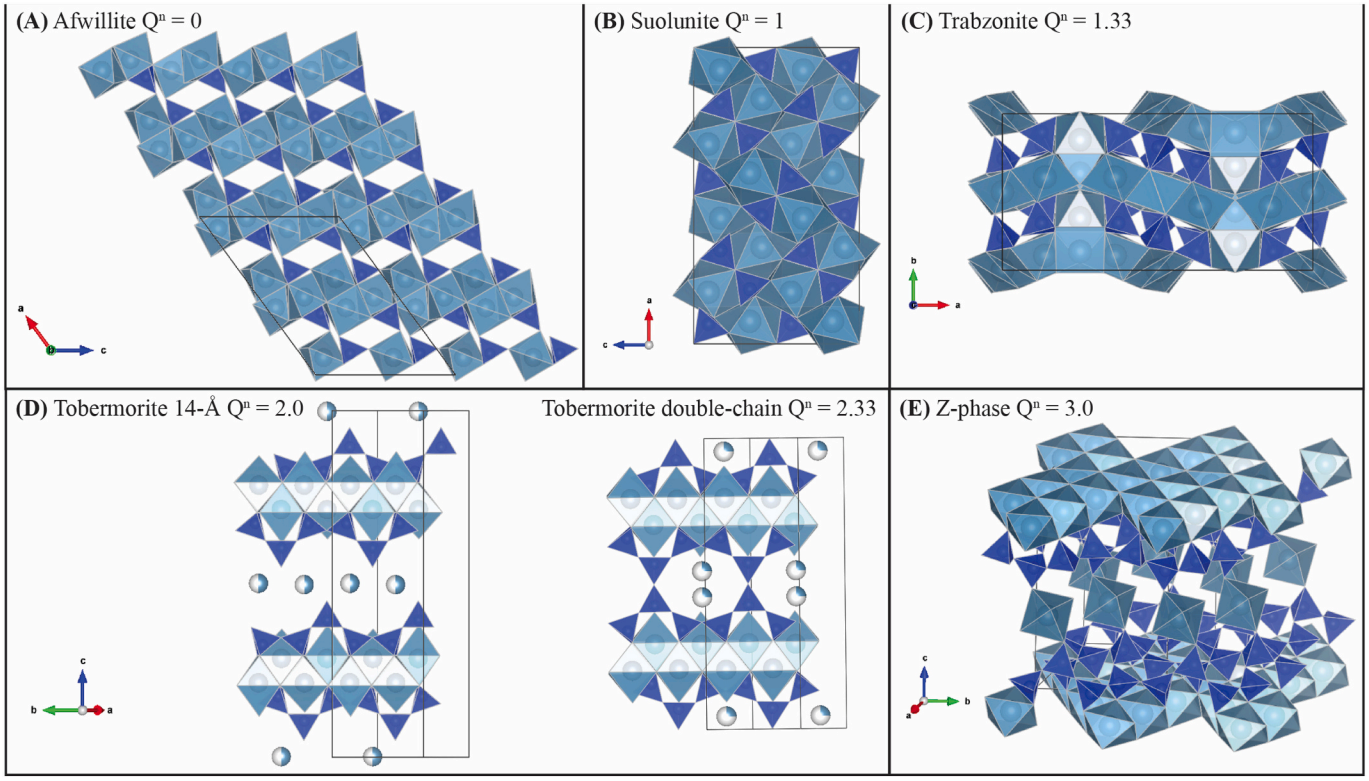

Fig. 6. The crystal structure of typical C-S-H minerals in increasing average Q^n: (A) afwillite, (B) suolunite, (C) trabzonite, (D) tobermorite, and (E) Z-phase. The outlined grey box indicates the unit cell of the crystal structure. Ca—O polyhedron is illustrated in light blue, and the silicate in dark blue; oxygen atoms at the corners of every polyhedron are omitted for clarity. The polyhedron for Ca with partial occupancy in tobermorite is not drawn. In all C-S-H minerals, Si-O-Ca bonding is present, and the SiO_4 tetrahedron and CaO_x polyhedron are most frequently corner-sharing. A small amount of edge-sharing of SiO_4 and CaO_x forms independently of Ca/Si molar ratio – for one SiO_4, sharing one of the six edges is most common, and maximally sharing three edges occurs in suolunite. In contrast, edge-sharing of adjacent SiO_4 does not exist in any presently examined minerals. (For interpretation of the references to color in this figure legend, the reader is referred to the web version of this article.)

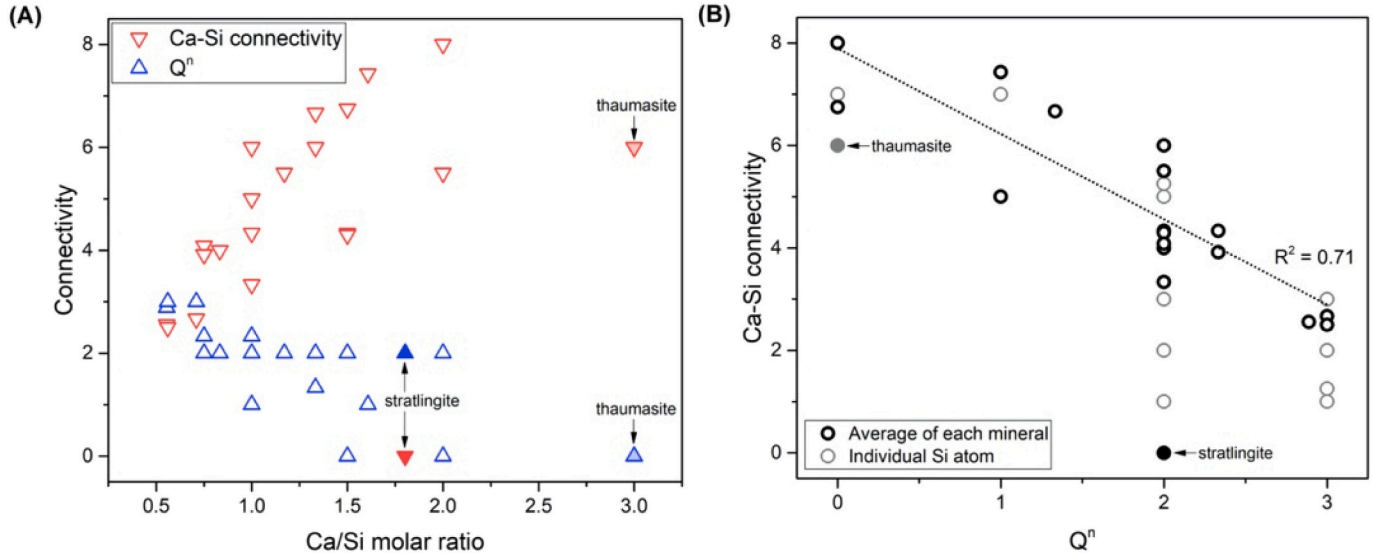

Fig. 7. (A) The relationship between Ca/Si and the average Ca—Si (red) connectivity or Q^n (blue) of each mineral. The point corresponding to strätlingite and thaumasite are indicated with the darker and lighter filled triangles, respectively. Note that Ca/Si ratio is substituted with (Ca + Na)/Si in pectolite, (Ca + Mn)/Si in poldervaartite, and (Ca + Na)/(Si + Al) in gyrolite. (B) The relationship between Ca—Si connectivity and Q^n. The grey hollow circles represent individual Si atoms; the black hollow circles represent the average of Si atoms in each mineral. Strätlingite is excluded from the correlation. (For interpretation of the references to color in this figure legend, the reader is referred to the web version of this article.)

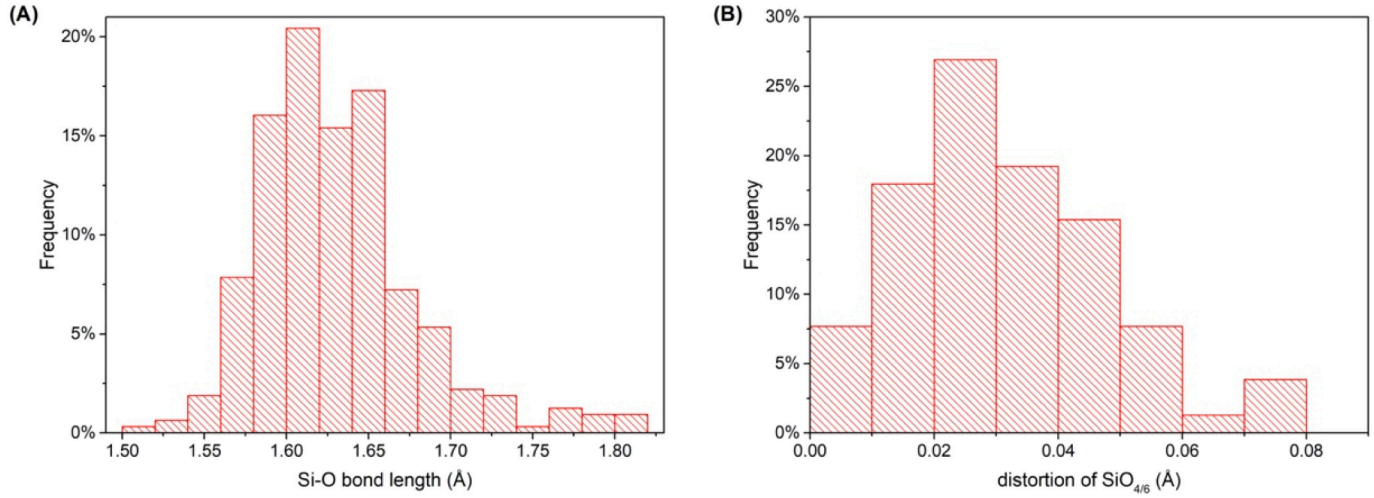

Fig. 8. Statistics of (A) Si—O bond length and (B) the distortion of each SiO_4 or SiO_6 expressed by the standard deviation of the lengths of the four/six Si—O bonds forming the SiO_4/SiO_6. The numbers of different Si atoms and Si—O bonds are 79 and 318, respectively.

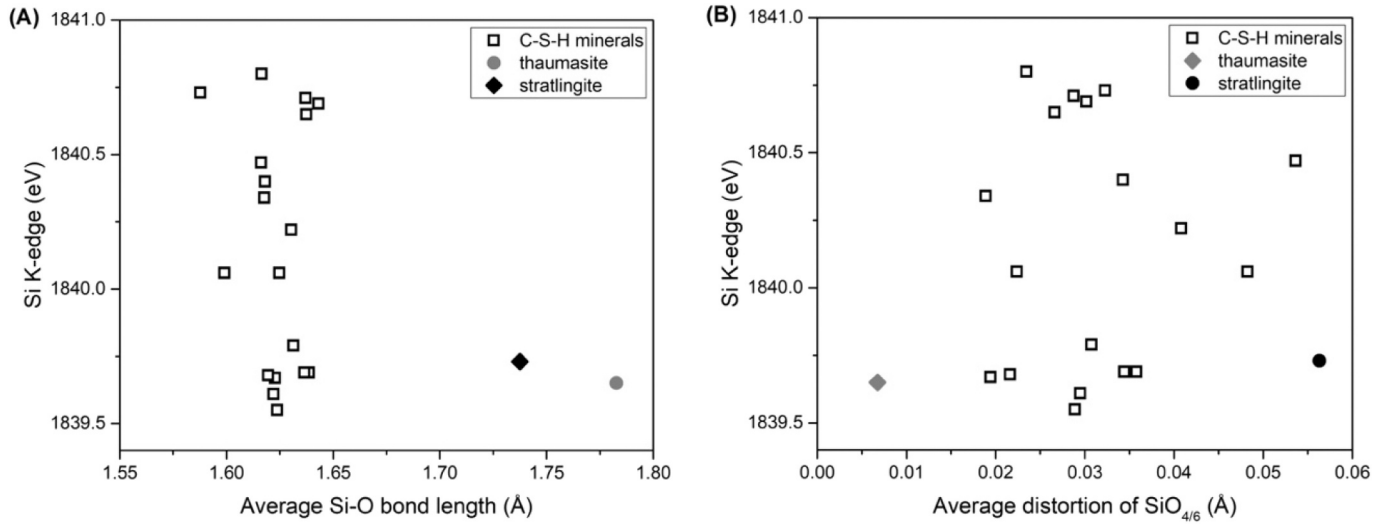

Fig. 9. Relationship between Si K-edge and (A) average Si—O bond length of each mineral and (B) average distortion (i.e., the standard deviation of the Si—O bond lengths) of SiO_4 or SiO_6 of each mineral.

exists when phases with similar structures are compared. For example, as Ca/Si of C-S-H(I) decreases, their Si—O bond length decreases while the Si K-edge increases [51]. The results here are still useful for distinguishing silicates in complex systems as peaks B, C, D, and E and other peaks of XANES spectra can be used as fingerprints.

3.4. Si K-edge of Al-tobermorite and nanocrystalline C-S-H

Fig. 10 shows the Si K-edge XANES spectra of tobermorite, nanocrystalline C-S-H (interchangeably used with the term C-S-H I), and metakaolin for comparison. Tobermorite is widely assumed as the structural model for the nanocrystalline C-S-H. Indeed, the exact alignment of the post-edge minor peak D between nanocrystalline C-S-H and different tobermorites provides strong support of their structural similarity in the neighbor shells. In contrast, the Si K-edge XANES spectrum of metakaolin lacks the shoulder peak C and the post-edge minor peak D, and its diffuse hump E appears to be more bimodal rather than skewed to the right compared to the other spectra in Fig. 10 (see arrows). These differences indicate the distinctions in the neighbor atomic shells between metakaolin and tobermorite-like phases (e.g., Al-tobermorite and nanocrystalline C-S-H).

The Si K-edge of metakaolin is ~0.1 eV lower than that of the double-chain tobermorite. This difference in the Si K-edge energy is explained by a competition between the effects of their Q^n and different cation species. On one hand, in ^{29}Si NMR, the signal from metakaolin peaks at Q^4(1Al) with a very broad range of chemical shifts [82]; the double-chain tobermorite is Q^4-free with Q^3:Q^2 ratio of 1:2 – regarding the abovementioned trend, the higher Q^n implies higher Si K-edge energy. On the other hand, the heavier cation (e.g., Ca^{2+}) has the effect of shifting the Si K-edge to higher energy compared to the lighter cation [58]. Therefore, the greater average Q^n yet the absence of Ca^{2+} in metakaolin could rationalize its slightly lower Si K-edge than tobermorite. Nonetheless, by looking at the (Al-)tobermorite alone, the increasing substitution of Si with Al leads to shifts in Si K-edge to higher energies. Therefore, the comparison between metakaolin and the tobermorite implicates the complexity in the multiple factors simultaneously governing the Si K-edge. This complexity suggests that a correlation of the Si K-edge to the phases' local chemical environment should be carefully drawn by isolating one variable (e.g., Q^n species, Al substitution, and cation species) from others.

The Si K-edge of the C-S-H phases is plotted against Ca/Si molar ratio, Q^n connectivity, and Ca—Si connectivity in Fig. 11A-C,

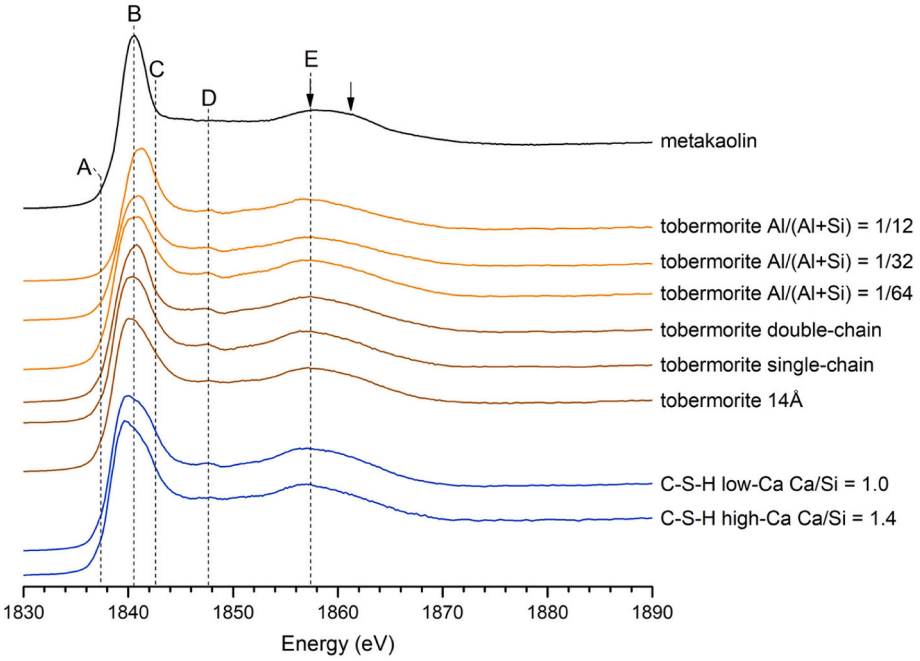

Fig. 10. Si K-edge XANES spectra of metakaolin, Al-tobermorite, tobermorites, and nanocrystalline C-S-Hs (low-Ca Ca/Si = 1.0 and high-Ca Ca/Si = 1.4). The energy of the Si K-edge is indicated with the arrow; the dash lines are drawn for eye guidance. The spectrum of C-S-H high-Ca with Ca/Si = 1.4 is reproduced from [81].

respectively, with an emphasis on (Al-)tobermorite and nanocrystalline C-S-H. The Si K-edge of nanocrystalline C-S-Hs falls within the Si K-edge range of C-S-H minerals at their comparable Ca/Si (Fig. 11A). A decrease in the Si K-edge with increased Ca/Si is observed here, consistent with a previous XPS study [80] that the Si 2p BE decreases with increasing Ca/Si of the nanocrystalline C-S-H, both related to higher residual negative charges on SiO_4 or reduced effective charge on Si at higher Ca/Si. The double-chain tobermorite and the Al-tobermorite (Al/(Al + Si) = 1/64) possess comparable Ca/Si and Si K-edge. This observation is sensible because the Al-tobermorite (Al/(Al + Si) = 1/64) is also highly cross-linked and shares great structural similarity with the double-chain tobermorite. At higher substitution levels, the Si K-edge of Al-tobermorite increases and no longer falls within the range of the C-S-H minerals Si K-edges. The present trend in tobermorite-like phases – the substitution of SiO_4 with AlO_4 shifts the Si K-edge to higher energies – is consistent with that in nanocrystalline C-S-H observed our previous study [51]. The Al-uptake induced Si K-edge energy increase can be applied to differentiate Al content in phases with similar structures in complex systems.

In Fig. 11B, the measured Si K-edge of nanocrystalline C-S-H and Al-tobermorite is plotted against their respective possible range of Q^n. The high-Ca C-S-H I with Ca/Si = 1.4 is non-cross-linked and contains a considerable number of vacant bridging sites, resulting in the dominancy of Q^1 species. Thus, the Q^n range 1.0–1.5 is assigned to the high-Ca C-S-H I. The low-Ca C-S-H I with Ca/Si = 1.0 is also non-cross-linked yet contains only a limited number of vacant bridging sites. Thus, Q^n near but below 2.0 is assigned to the low-Ca C-S-H I. The narrow Q^n range of the Al-tobermorite is determined from ^{29}Si NMR results. The Si K-edge of nanocrystalline C-S-Hs are comparable to those of the C-S-H minerals with similar Q^n; and it indeed shifts toward higher energy with increasing Q^n, in agreement with the trend of the C-S-H minerals. In accordance with the positive correlation, the cross-linked double-chain tobermorite with an average Q^n of 2.33 possesses a higher Si K-edge than single-chain 11 Å and 14 Å tobermorite, which are both non-cross-linked and with only Q^2. The highly similar Al-tobermorite (Al/(Al + Si) = 1/64) and double-chain tobermorite overlap on the scatter plot while the two Al-tobermorite at higher Al/(Al + Si) ratios possess noticeably elevated Si K-edge despite comparable Q^n of the four samples. At Al/(Al + Si) = 1/12, the Si K-edge increased by ~0.4 eV relative to the double-chain tobermorite. Thus, with the influence of Q^n on Si K-edge eliminated, it is reaffirmed that the substitution of Si with Al, alone, contributes to shift the Si K-edge to higher energy in the system of C-S-H minerals.

While the Si K-edge and the Si 2p BE often shift in the same direction due to changes in the coordination environment of Si (e.g., Q^n or Ca/Si), the Si 2p BE decreases with increasing substitution of Si with Al in Al-tobermorite [53] – opposite to the trend in the Si K-edge shift of Al-tobermorite. At the studied Al contents, the substitution of Si with Al has minimal influence on the average Q^n of the Al-tobermorite (which remains highly cross-linked), the substitution of O^{2-} with OH^- balances the charge, and the bulk Ca/(Al + Si) is maintained. Ca, with low electronegativity, has great effect on reducing the effective charge on Si and thus reducing the Si K-edge; whereas, hydrogen, with electronegativity higher than Si, has the opposite effect. From there, the observed shift of the Si K-edge to higher energy with increasing Al content can be explained: the interlayer Ca preferentially bonds to the cross-linked aluminate instead of silicates, and the silicate then forms Si-OH for charge balancing [21]. As a result, for an Si atom in Al-tobermorite, the number of the second-shell Ca decreases while the number of the second-shell proton increases – the effective charge of the central Si thus increases, and the Si K-edge shifts to higher energy accordingly. Since the substitution of Si with Al causes complex simultaneous changes to the coordination environment of the pairing Si and the cross-linking site Si (as well as the few bridging site Si), the different degree of the influence of Si—O—Al, Si-OH, and Si—O—Ca on the shifts in the Si K-edge and the Si 2p BE may account for the overall opposite trends.

In Fig. 11C, the Ca—Si connectivity of Al-tobermorite is assigned according to the double-chain tobermorite as the low substitution of Si with Al should present limited influence on the Ca sites in the crystal structure. In non-cross-linked nanocrystalline C-S-H, the Ca—Si connectivity of a pairing site silicate is ~5, if the adjacent bridging site is occupied, or ~ 6, if it is vacant; the Ca—Si connectivity of a bridging site silicate is ~1. Thus, based on the estimated Q^n, the Ca—Si connectivity ~4 and ~5.5 are assigned to the low-Ca and high-Ca nanocrystalline C-S-H samples, respectively. The Si K-edge energy of the nanocrystalline C-S-Hs again falls within the trend of the C-S-H minerals as a function of

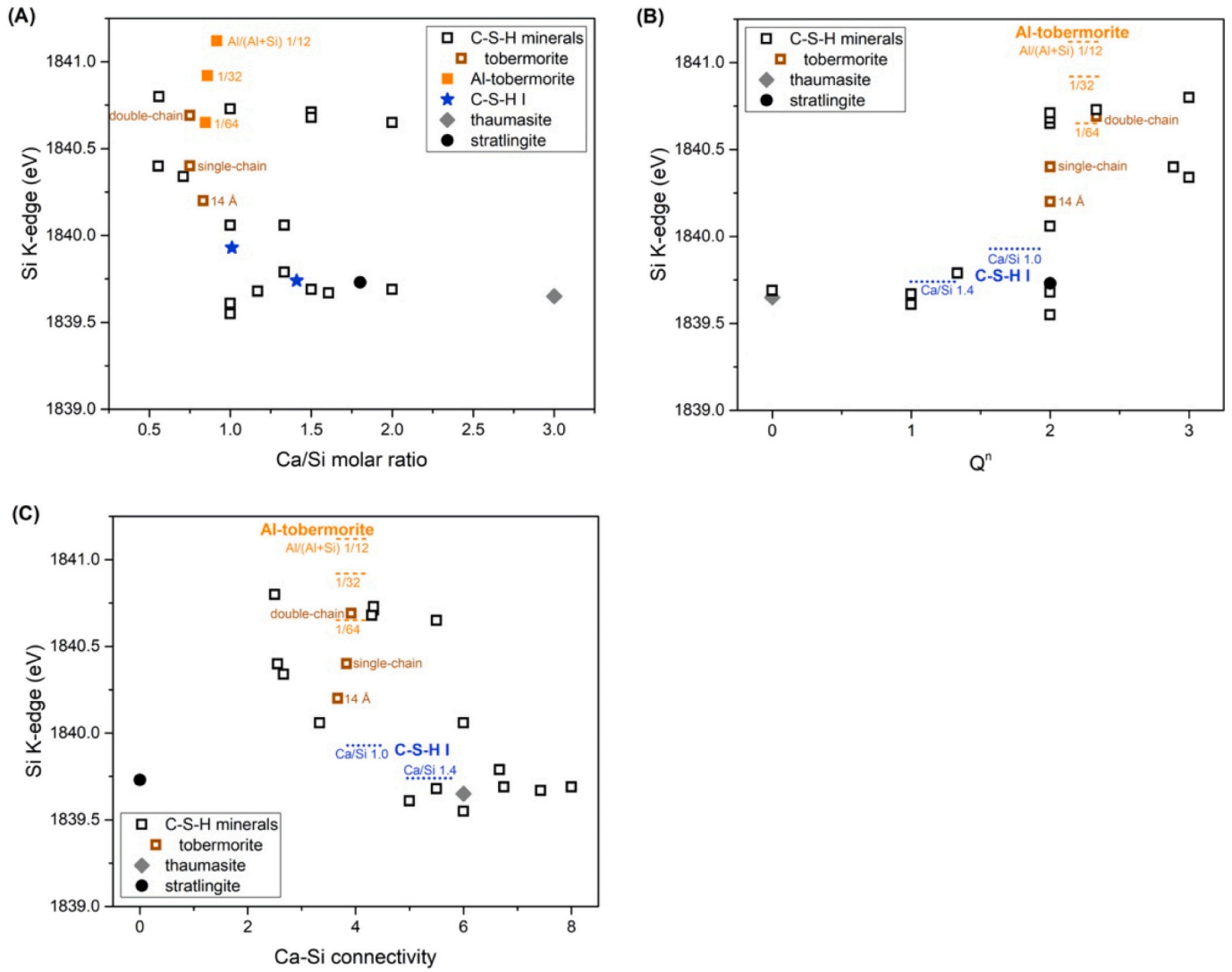

Fig. 11. Relationship between the Si K-edge and (A) Ca/Si molar ratio, (B) average Q^n, and (C) Ca—Si connectivity of each mineral, with an emphasis on Al-tobermorite (yellow), tobermorite (brown), and C-S-H (blue). Each dash line in (B) and (C) represents the designated range of average Q^n or average Ca—Si connectivity of the specific synthetic Al-tobermorite or C-S-H sample. (For interpretation of the references to color in this figure legend, the reader is referred to the web version of this article.)

Ca—Si connectivity. The Si K-edge energy of Al-tobermorite exceeds that of the C-S-H minerals with comparable Ca—Si connectivity, explained by the influence of Al incorporation.

In general, the relationships between the Si K-edge energy of nanocrystalline C-S-H and its local environment of SiO_4 agree well with the trends in the C-S-H minerals. Accordingly, a comparison of the Q^n (i.e., silicate polymerization) and Ca—Si connectivity (i.e., Ca/Si ratio here) between different C-S-H samples could be achieved through a comparison of their different Si K-edge (see Tables S1–S4 in SI).

3.5. Si K-edge of blast-furnace slags and synthetic slags

In Fig. 12, the Si K-edge XANES spectra of slags are compared with low-Ca C-S-H I (Ca/Si = 1.0). The former and the latter are representative of the raw material/precursor and the reaction product in cement-based/alkali-activated materials, respectively. The Si K-edge XANES spectra of all the examined slags possess similar presence of the shoulder peak and similar post-edge features, suggesting the comparable medium-range structures among all these samples from different origins. The Si K-edge energies of the commercial GGBFS (AU, CAN, UAE, CN, and US) vary within 1839.1 ± 0.1 eV while that of the synthetic slag samples EU are at slightly higher energies (~1839.5–1839.7 eV). This systematically higher Si K-edge of the synthetic than the commercial slags may be attributed to the higher content of heavier cation (e.g., Mn and Fe) in the former or difference in the additional heat treatment.

The element compositions of the EU slags are strictly controlled; the only variation is in the level of substitution of Si with Al. Among the three synthetic slags, the Si K-edge is positively correlated to the Al content (~0.2 eV increase in Si K-edge as Al_2O_3 content increases from 7% to 17% while total SiO_2 plus Al_2O_3 content is maintained) – the effect of Al substitution on the Si K-edge of slags is in accordance with that of tobermorite. However, this Al substitution-related shift in Si K-edge could not be observed in the commercial GGBFS, and other spectral differences among the commercial GGBFS (e.g., varying shoulder peak intensity) also could not be explained by the different proportioning between the major elements (i.e., Ca, Mg, Si, and Al). These unaccountable slight differences between the largely similar Si K-edge spectra of the different GGBFS are explained by the complex composition and the presence of various minor elements.

A clear distinction is present between the Si K-edge XANES spectra of slags and a nanocrystalline C-S-H, making it feasible to locally identify slags and C-S-H in cementitious systems, e.g., using XANES-based STXM

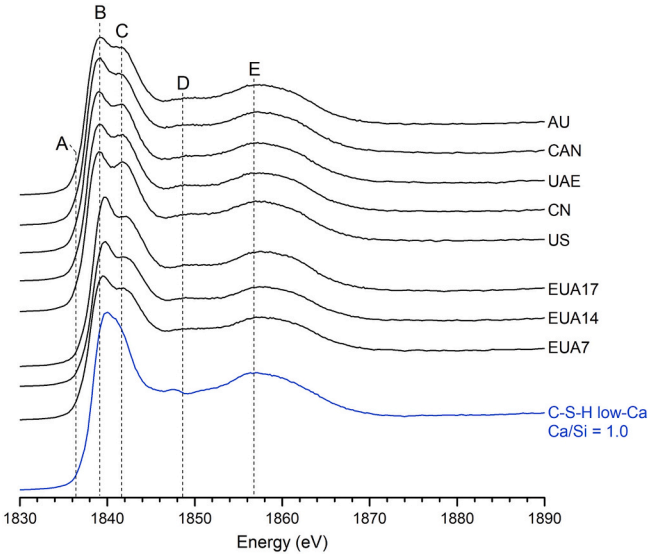

Fig. 12. Si K-edge XANES spectra of slags and nanocrystalline low-Ca C-S-H I (Ca/Si = 1.0).

[44,52] with the spatial resolution down to 8 nm. STXM has been successfully applied to locally identify different phases in calcium aluminate and calcium silicate hydration systems [40,49,50]. Note that, distinguishing these phases in complex cementitious systems using bulk XANES techniques with peak deconvolutions is still challenging. The Si K-edge of slags is generally at lower energies compared to the nanocrystalline C-S-H, which could be explained by the lower Q^n species of silicate in slags (mainly Q^1 with a broad range of chemical shifts as Q^0-Q^2 in ^{29}Si NMR [56]) than in the nanocrystalline C-S-H (majorly Q^1 and Q^2) [83]. In addition, the weaker shoulder peak C of nanocrystalline C-S-H implicates its lower Ca/Mn-Si connectivity compared to slags. The distinct position of the post-edge peak D between slags (~1848.6 eV) and nanocrystalline C-S-H (~1847.5 eV) is another signature for local phase identifications.

4. Conclusions

A database of Si K-edge XANES spectra of different C-S-H related minerals, different tobermorites, nanocrystalline C-S-H, amorphous (calcium) aluminosilicates, and other silicates is presented in the study. The spectra of different Si-rich phases exhibit multiple peaks and shoulders and can be used as fingerprints for locally identifying different Si phases or differentiating phases with various compositions in complex cementitious systems using X-ray microspectroscopy (e.g., STXM with spatial resolution of 8–10 nm) [44]. Important implications of the spectral features (i.e., the Si K-edge position, presence of shoulder peaks, and post-edge patterns) on the coordination environment of Si were learned.

In the C-S-H related minerals, the Si K-edge energy is most significantly influenced by the second nearest neighbor atomic shell neighboring to an Si atom. Q^n (ranging from Q^0 to Q^3) is in a clear positive correlation to the Si K-edge energy; the Ca—Si connectivity (ranging from 0 to 8) is in a negative linear correlation to the Si K-edge energy, and the presence of more second-shell Ca atoms typically intensifies the shoulder at ~2–3 eV above the Si K-edge. In addition, the substitution of Si with Al increases the Si K-edge energy in (Al-)tobermorite. However, Si K-edge shows no obvious correlation with Ca/Si molar ratio, the average Si—O bond length, or distortion within SiO_4 tetrahedra of the C-S-H related minerals.

This study also highlights the influences of complexity in structures on the Si K-edge energy. In strätlingite, the proton in the second nearest neighbor shell of Si weakens the Si—O bond, and thus, strätlingite exhibits its exclusion from the correlation between Si K-edge energy and Ca—Si connectivity. Metakaolin with Q^4 connectivity has a relatively low Si K-edge energy due to the lack of heavier cation species (e.g., Ca). Commercial blast-furnace slags with various compositions exhibits similar Si K-edge energy and other absorption features. Synthetic blast-furnace slags show higher Si K-edge energy compared to the commercial slag, possibly due to the existence of cations or high temperature re-treatment. Additionally, highly similar post-edge patterns (e.g., between (Al-)tobermorite and nanocrystalline C-S-H; between GGBFS from different origins) is a signature for similar medium-range structures.

The relationship between the Si K-edge energy and the Si coordination environment in the C-S-H minerals is readily applicable to the nanocrystalline C-S-H. The different post-edge patterns characteristic to each phase, as fingerprints, facilitate the local distinguishing between metakaolin, GGBFS, and the crystalline and poorly crystalline C-S-Hs – the raw materials and reaction products in siliceous binder systems. These capabilities give merits to XANES, particularly STXM, as a powerful tool for the study of cementitious materials that consists of complex cement/gel systems.

CRediT authorship contribution statement

Jiaqi Li: Conceptualization, Methodology, Investigation, Validation, Visualization, Writing – original draft. **Wenxin Zhang:** Investigation, Visualization, Writing – original draft. **Krassimir Garbev:** Investigation, Validation, Writing – review & editing. **Paulo J.M. Monteiro:** Validation, Writing – review & editing, Supervision, Funding acquisition.

Declaration of competing interest

The authors declare that they have no known competing financial interests or personal relationships that could have appeared to influence the work reported in this paper.

Acknowledgement

Dr. Claire White in Princeton University, Dr. Barbara Lothenbach in EMPA, and Dr. Kemal Celik in New York University Abu Dhabi are thanked for providing slag samples. Yejin Emily You at Berkeley is thanked for assisting the synthesis of nanocrystalline C-S-H. This work was founded by the Republic of Singapore's National Research Foundation through a grant to the Berkeley Education Alliance for Research in Singapore (BEARS) for the Singapore-Berkeley Building Efficiency and Sustainability in the Tropics (SinBerBEST) Program. We acknowledge the Paul Scherrer Institut, Villigen, Switzerland for provision of synchrotron radiation beamtime at beamline PHOENIX of the SLS and would like to thank Dr. Thomas Huthwelker for assistance.

Appendix A. Supplementary data

Supplementary data to this article can be found online at https://doi.org/10.1016/j.cemconres.2021.106376.

References

[1] H.F.W. Taylor, Cement Chemistry, Thomas Telford, 1997.
[2] S.A. Miller, R.J. Myers, Environmental impacts of alternative cement binders, Environ. Sci. Technol. 54 (2) (2020) 677–686.
[3] J.L. Provis, Alkali-activated materials, Cem. Concr. Res. 114 (2018) 40–48.
[4] G.Q. Geng, R. Taylor, S. Bae, D. Hernandez-Cruz, D.A. Kilcoyne, A.H. Emwas, P.J. M. Monteiro, Atomic and nano-scale characterization of a 50-year-old hydrated C3S paste, Cem. Concr. Res. 77 (2015) 36–46.
[5] R.J. Myers, S.A. Bernal, J.D. Gehman, J.S. Deventer, J.L. Provis, The role of Al in cross-linking of alkali-activated slag cements, J. Am. Ceram. Soc. 98 (3) (2015) 996–1004.
[6] P. Duxson, J.L. Provis, G.C. Lukey, S.W. Mallicoat, W.M. Kriven, J.S.J. van Deventer, Understanding the relationship between geopolymer composition, microstructure and mechanical properties, Colloid Surf. A 269 (1–3) (2005) 47–58.

[7] J.S. Dolado, M. Griebel, J. Hamaekers, F. Heber, The nano-branched structure of cementitious calcium-silicate-hydrate gel, J. Mater. Chem. 21 (12) (2011) 4445–4449.
[8] R.J. Myers, S.A. Bernal, J.L. Provis, Phase diagrams for alkali-activated slag binders, Cem. Concr. Res. 95 (2017) 30–38.
[9] Y. Jeong, C.W. Hargis, S.-C. Chun, J. Moon, The effect of water and gypsum content on strätlingite formation in calcium sulfoaluminate-belite cement pastes, Constr. Build. Mater. 166 (2018) 712–722.
[10] C. Li, M.X. Wu, W. Yao, Eco-efficient cementitious system consisting of belite-ye'elimite-ferrite cement, limestone filler, and silica fume, ACS Sustain. Chem. Eng. 7 (8) (2019) 7941–7950.
[11] C. Li, M.X. Wu, W. Yao, Effect of coupled B/Na and B/Ba doping on hydraulic properties of belite-ye'elimite-ferrite cement, Constr. Build. Mater. 208 (2019) 23–35.
[12] C.J. Shi, A.F. Jimenez, A. Palomo, New cements for the 21st century: the pursuit of an alternative to Portland cement, Cem. Concr. Res. 41 (7) (2011) 750–763.
[13] H.-I. Hsiang, W.-S. Chen, W.-C. Huang, Pre-reaction temperature effect on C–S–H colloidal properties and xonotlite formation via steam assisted crystallization, Mater. Struct. 49 (3) (2016) 905–915.
[14] F. Méducin, C. Noïk, A. Rivereau, H. Zanni, Complementary analyses of a tricalcium silicate sample hydrated at high pressure and temperature, Cement Concr. Res. 32 (1) (2002) 65–70.
[15] G. Bell, J. Bensted, F.P. Glasser, Characterization of hydrothermally-treated calcium silicate and oilwell cement hydration products, Adv. Cem. Res. 2 (6) (1989) 61–72.
[16] G. Geng, Z. Shi, A. Leemann, C. Borca, T. Huthwelker, K. Glazyrin, I.V. Pekov, S. Churakov, B. Lothenbach, R. Dähn, Atomistic structure of alkali-silica reaction products refined from X-ray diffraction and micro X-ray absorption data, Cem. Concr. Res. 129 (2020) 105958.
[17] J. Moon, S. Speziale, C. Meral, B. Kalkan, S.M. Clark, P.J. Monteiro, Determination of the elastic properties of amorphous materials: case study of alkali–silica reaction gel, Cem. Concr. Res. 54 (2013) 55–60.
[18] E. Boehm-Courjault, S. Barbotin, A. Leemann, K. Scrivener, Microstructure, crystallinity and composition of alkali-silica reaction products in concrete determined by transmission electron microscopy, Cem. Concr. Res. 130 (2020) 105988.
[19] G. Geng, Z. Shi, A. Leemann, K. Glazyrin, A. Kleppe, D. Daisenberger, S. Churakov, B. Lothenbach, E. Wieland, R. Dähn, Mechanical behavior and phase change of alkali-silica reaction products under hydrostatic compression, Acta Crystallogr. Sect. B Struct. Sci. Cryst. Eng. Mater. 76 (4) (2020).
[20] G. Geng, R.N. Vasin, J. Li, M.J.A. Qomi, J. Yan, H.R. Wenk, P.J.M. Monteiro, Preferred orientation of calcium aluminosilicate hydrate induced by confined compression, Cem. Concr. Res. 113 (2018) 186–196.
[21] J. Li, W. Zhang, K. Garbev, G. Beuchle, P.J. Monteiro, Influences of cross-linking and Al incorporation on the intrinsic mechanical properties of tobermorite, Cem. Concr. Res. 136 (2020) 106170.
[22] J. Li, W. Zhang, P.J.M. Monteiro, The structure and intrinsic mechanical properties of nanocrystalline calcium silicate hydrate, ACS Sustain. Chem. Eng. 8 (33) (2020) 12453–12461.
[23] H.-R. Wenk, A.G. Bulakh, Minerals: Their Constitution and Origin, Second ed., Cambridge University Press, Cambridge, United Kingdom, 2016.
[24] J. Moon, S. Kim, S. Bae, S.M. Clark, Pressure-induced anomalous behavior of thaumasite crystal, J. Am. Ceram. Soc. 103 (6) (2020) 3763–3775.
[25] A. Simunek, J. Vackar, G. Wiech, Local s, p and d charge distributions and X-ray emission bands of SiO_2: alpha-quartz and stishovite, J. Phys. Condens. Matter 5 (7) (1993) 867.
[26] R. Angel, Transformation of fivefold-coordinated silicon to octahedral silicon in calcium silicate, $CaSi_2O_5$, Am. Miner. J. Earth Planet. Mater. 82 (7–8) (1997) 836–839.
[27] O. Mikhailova, A. del Campo, P. Rovnanik, J. Fernández, M. Torres-Carrasco, In situ characterization of main reaction products in alkali-activated slag materials by Confocal Raman Microscopy, Cem. Concr. Compos. 99 (2019) 32–39.
[28] S. Ortaboy, J. Li, G. Geng, R.J. Myers, P.J. Monteiro, R. Maboudian, C. Carraro, Effects of CO_2 and temperature on the structure and chemistry of C–(A–)S–H investigated by Raman spectroscopy, RSC Adv. 7 (77) (2017) 48925–48933.
[29] I.G. Richardson, Tobermorite/jennite- and tobermorite/calcium hydroxide-based models for the structure of C-S-H: applicability to hardened pastes of tricalcium silicate, beta-dicalcium silicate, Portland cement, and blends of Portland cement with blast-fumace slag, metakaolin, or silica fume, Cement Concr. Res. 34 (9) (2004) 1733–1777.
[30] J. Ibanez, L. Artus, R. Cusco, A. Lopez, E. Menendez, M.C. Andrade, Hydration and carbonation of monoclinic C2S and C3S studied by Raman spectroscopy, J. Raman Spectrosc. 38 (1) (2007) 61–67.
[31] L. Black, Raman spectroscopy of cementitious materials, Spectrosc. Prop. Inorg. Organomet. Compd 40 (2009) 72–127.
[32] B. Lothenbach, G. Le Saout, M. Ben Haha, R. Figi, E. Wieland, Hydration of a low-alkali CEM III/B-SiO_2 cement (LAC), Cem. Concr. Res. 42 (2) (2012) 410–423.
[33] E.T. Rodriguez, I.G. Richardson, L. Black, E. Boehm-Courjault, A. Nonat, J. Skibsted, Composition, silicate anion structure and morphology of calcium silicate hydrates (C-S-H) synthesised by silica-lime reaction and by controlled hydration of tricalcium silicate (C3S), Adv. Appl. Ceram. 114 (7) (2015) 362–371.
[34] M.D. Andersen, H.J. Jakobsen, J. Skibsted, Incorporation of aluminum in the calcium silicate hydrate (C-S-H) of hydrated Portland cements: a high-field Al-27 and Si-29 MAS NMR investigation, Inorg. Chem. 42 (7) (2003) 2280–2287.
[35] M. Zajac, J. Skibsted, J. Skocek, P. Durdzinski, F. Bullerjahn, M.B. Haha, Phase assemblage and microstructure of cement paste subjected to enforced, wet carbonation, Cem. Concr. Res. 130 (2020) 105990.
[36] E. Pustovgar, R.P. Sangodkar, A.S. Andreev, M. Palacios, B.F. Chmelka, R.J. Flatt, J.-B.D.E. de Lacaillerie, Understanding silicate hydration from quantitative analyses of hydrating tricalcium silicates, Nat. Commun. 7 (1) (2016) 1–9.
[37] A. Kumar, B.J. Walder, A.K. Mohamed, A. Hofstetter, B. Srinivasan, A.J. Rossini, K. Scrivener, L. Emsley, P. Bowen, The atomic-level structure of cementitious calcium silicate hydrate, J. Phys. Chem. C 121 (32) (2017) 17188–17196.
[38] B. Ma, A. Fernandez-Martinez, S. Grangeon, C. Tournassat, N. Findling, S. Carrero, D. Tisserand, S. Bureau, E. Elkaim, C. Marini, G. Aquilanti, A. Koishi, N.C.M. Marty, L. Charlet, Selenite uptake by Ca-Al LDH: a description of intercalated anion coordination geometries, Environ. Sci. Technol. 52 (3) (2018) 1624–1632.
[39] B. Ma, A. Fernandez-Martinez, B. Made, N. Findling, E. Markelova, E. Salas-Colera, T.G.G. Maffeis, A.R. Lewis, D. Tisserand, S. Bureau, L. Charlet, XANES-based determination of redox potentials imposed by steel corrosion products in cement-based media, Environ. Sci. Technol. 52 (20) (2018) 11931–11940.
[40] P.J.M. Monteiro, G.Q. Geng, D. Marchon, J.Q. Li, P. Alapati, K.E. Kurtis, M.J. A. Qomi, Advances in characterizing and understanding the microstructure of cementitious materials, Cem. Concr. Res. 124 (2019) 105806.
[41] E. Wieland, R. Dahn, M. Vespa, B. Lothenbach, Micro-spectroscopic investigation of Al and S speciation in hardened cement paste, Cem. Concr. Res. 40 (6) (2010) 885–891.
[42] S. Bae, R. Taylor, D. Kilcoyne, J. Moon, P.J.M. Monteiro, Effects of incorporating high-volume fly ash into Tricalcium silicate on the degree of silicate polymerization and aluminum substitution for silicon in calcium silicate hydrate, Materials 10 (2) (2017).
[43] F. Meirer, J. Cabana, Y. Liu, A. Mehta, J.C. Andrews, P. Pianetta, Three-dimensional imaging of chemical phase transformations at the nanoscale with full-field transmission X-ray microscopy, J. Synchrotron Radiat. 18 (5) (2011) 773–781.
[44] D.A. Shapiro, S. Babin, R.S. Celestre, W. Chao, R.P. Conley, P. Denes, B. Enders, P. Enfedaque, S. James, J.M. Joseph, An ultrahigh-resolution soft X-ray microscope for quantitative analysis of chemically heterogeneous nanomaterials, Sci. Adv. 6 (51) (2020), eabc4904.
[45] S. Bae, C. Meral, J.-e. Oh, J. Moon, M. Kunz, P.J. Monteiro, Characterization of morphology and hydration products of high-volume fly ash paste by monochromatic scanning X-ray micro-diffraction (μ-SXRD), Cem. Concr. Res. 59 (2014) 155–164.
[46] Z. Wang, Q. Yu, F. Gauvin, P. Feng, R. Qianping, H. Brouwers, Nanodispersed TiO_2 hydrosol modified Portland cement paste: the underlying role of hydration on self-cleaning mechanisms, Cem. Concr. Res. 136 (2020) 106156.
[47] P. Stemmermann, K. Garbev, B. Gasharova, G. Beuchle, M. Haist, T. Divoux, Chemo-mechanical characterization of hydrated calcium-hydrosilicates with coupled Raman-and nanoindentation measurements, Appl. Geochem. 118 (2020) 104582.
[48] P. Hansen, R. Brydson, D. McComb, I. Richardson, EELS fingerprint of Al-coordination in silicates, Microsc. Microanal. Microstruct. 5 (3) (1994) 173–182.
[49] J. Li, G. Geng, W. Zhang, Y.S. Yu, D.A. Shapiro, P.J.M. Monteiro, The hydration of beta- and alpha(H)′-dicalcium silicates: an X-ray spectromicroscopic study, ACS Sustain. Chem. Eng. 7 (2) (2019) 2316–2326.
[50] S. Bae, R. Taylor, D. Hernandez-Cruz, S. Yoon, D. Kilcoyne, P.J.M. Monteiro, Soft X-ray Spectromicroscopic investigation of synthetic C-S-H and C3S hydration products, J. Am. Ceram. Soc. 98 (9) (2015) 2914–2920.
[51] J. Li, G. Geng, R. Myers, Y.S. Yu, D. Shapiro, C. Carraro, R. Maboudian, P.J. M. Monteiro, The chemistry and structure of calcium (alumino) silicate hydrate: a study by XANES, ptychographic imaging, and wide- and small-angle scattering, Cem. Concr. Res. 115 (2019) 367–378.
[52] A.L.D. Kilcoyne, T. Tyliszczak, W.F. Steele, S. Fakra, P. Hitchcock, K. Franck, E. Anderson, B. Harteneck, E.G. Rightor, G.E. Mitchell, A.P. Hitchcock, L. Yang, T. Warwick, H. Ade, Interferometer-controlled scanning transmission X-ray microscopes at the advanced light source, J. Synchrotron Radiat. 10 (2003) 125–136.
[53] L. Black, A. Stumm, K. Garbev, P. Stemmermann, K.R. Hallam, G.C. Allen, X-ray photoelectron spectroscopy of aluminium-substituted tobermorite, Cem. Concr. Res. 35 (1) (2005) 51–55.
[54] J. Moon, S. Yoon, P.J.M. Monteiro, Mechanical properties of jennite: a theoretical and experimental study, Cem. Concr. Res. 71 (2015) 106–114.
[55] K. Gong, C.E. White, Impact of chemical variability of ground granulated blast-furnace slag on the phase formation in alkali-activated slag pastes, Cem. Concr. Res. 89 (2016) 310–319.
[56] M.B. Haha, B. Lothenbach, G. Le Saout, F. Winnefeld, Influence of slag chemistry on the hydration of alkali-activated blast-furnace slag—part II: effect of Al_2O_3, Cem. Concr. Res. 42 (1) (2012) 74–83.
[57] D.W. Gardner, J. Li, A. Morshedifard, S. Masoumi, M.J. Abdolhosseini Qomi, P. J. Monteiro, R. Maboudian, C. Carraro, Silicate bond characteristics in calcium-silicate-hydrates determined by high pressure Raman spectroscopy, J. Phys. Chem. C 124 (33) (2020) 18335–18345.
[58] D. Li, G.M. Bancroft, M.E. Fleet, X.H. Feng, Silicon K-edge Xanes spectra of silicate minerals, Phys. Chem. Miner. 22 (2) (1995) 115–122.
[59] D. Li, G.M. Bancroft, M. Kasrai, M.E. Fleet, R.A. Secco, X.H. Feng, K.H. Tan, B. X. Yang, X-ray-absorption spectroscopy of silicon dioxide (SiO_2) polymorphs — the structural characterization of opal, Am. Mineral. 79 (7–8) (1994) 622–632.
[60] D. Li, M.E. Fleet, G.M. Bancroft, M. Kasrai, Y.M. Pan, Local-structure of Si and P in SiO_2-P_2O_5 and Na_2O-SiO_2-P_2O_5 glasses — a Xanes study, J. Non-Cryst. Solids 188 (1–2) (1995) 181–189.

[61] H. Taylor, The crystal structure of killalaite, Mineral. Mag. 41 (319) (1977) 363–369.
[62] Z. Ma, N. Shi, G. Mou, L. Liao, Crystal structure refinement of suolunite and its significance to the cement techniques, Chin. Sci. Bull. 44 (23) (1999) 2125–2130.
[63] S. Merlino, E. Bonaccorsi, T. Armbruster, The real structure of tobermorite 11 angstrom: normal and anomalous forms, OD character and polytypic modifications, Eur. J. Miner. 13 (3) (2001) 577–590.
[64] Y. Dai, G.E. Harlow, A.R. McGhie, Poldervaartite, Ca ($Ca_{0.5}Mn_{0.5}$)(SiO_3OH)(OH), a new acid nesosilicate from the Kalahari manganese field, South Africa: crystal structure and description, Am. Miner. 78 (9–10) (1993) 1082–1087.
[65] M. Buerger, C. Prewitt, The crystal structures of wollastonite and pectolite, Proc. Natl. Acad. Sci. USA 47 (12) (1961) 1884.
[66] R.K. Rastsvetaeva, N.V. Chukanov, A.E. Zadov, Refined structure of afwillite from the northern Baikal region, Crystallogr. Rep+. 54 (3) (2009) 418–422.
[67] J. Gard, H. Taylor, The crystal structure of foshagite, Acta Crystallogr. 13 (10) (1960) 785–793.
[68] S. Merlino, Gyrolite — its crystal-structure and crystal-chemistry, Mineral. Mag. 52 (366) (1988) 377–387.
[69] Y. Dai, J.E. Post, Crystal structure of hillebrandite: a natural analogue of calcium silicate hydrate (CSH) phases in Portland cement, Am. Mineral. 80 (7–8) (1995) 841–844.
[70] S. Merlino, Okenite, $Ca_{10}Si_{18}O_{46.18}H_2O$ — the 1st example of a chain and sheet silicate, Am. Miner. 68 (5–6) (1983) 614–622.
[71] J. Pluth, J. Smith, The crystal structure of scawtite, Ca_7 (Si_6O_{18})(CO_3)·$2H_2O$, Acta Crystallogr. Sect. B Struct. Crystallogr. Cryst. Chem. 29 (1) (1973) 73–80.
[72] R. Rinaldi, M. Sacerdoti, E. Passaglia, Strätlingite: crystal structure, chemistry, and a reexamination of its polytpye vertumnite, Eur. J. Mineral. (1990) 841–850.
[73] R. Edge, H. Taylor, Crystal structure of thaumasite, [Ca_3Si $(OH)_{6.12}$ H_2O](SO_4) (CO_3), Acta Crystallogr. Sect. B Struct. Crystallogr. Cryst. Chem. 27 (3) (1971) 594–601.
[74] E. Bonaccorsi, S. Merlino, Crystal chemistry and structural arrangements of 'normal' and 'anomalous' tobermorite 11 angstrom, Appl. Miner. 1–2 (2000) 735–738.
[75] S. Merlino, E. Bonaccorsi, A.R. Kampf, Tobermorite 14 angstrom: crystal structure and OD character, Appl. Miner. 1–2 (2000) 859–861.
[76] S. Hamid, The crystal structure of the 11 Å natural tobermorite $Ca_{2.25}$ [$Si_3O_{7.5}(OH)_{1.5}$]·$1H_2O$, Zeitsch. Kristallogr.-Cryst. Mater. 154 (1–4) (1981) 189–198.
[77] T. Armbruster, B. Lazic, I. Galuskina, E. Galuskin, E. Gnos, K.M. Marzec, V. Gazeev, Trabzonite, $Ca_4[Si_3O_9(OH)]OH$: crystal structure, revised formula, new occurrence and relation to killalaite, Mineral. Mag. 76 (3) (2012) 455–472.
[78] C. Hejny, T. Armbruster, Polytypism in xonotlite $Ca_6Si_6O_{17}(OH)_2$, Z. Kristallogr. 216 (7) (2001) 396–408.
[79] L. Black, K. Garbev, P. Stemmermann, K.R. Hallam, G.C. Allen, Characterisation of crystalline C-S-H phases by X-ray photoelectron spectroscopy, Cem. Concr. Res. 33 (6) (2003) 899–911.
[80] L. Black, K. Garbev, G. Beuchle, P. Stemmermann, D. Schild, X-ray photoelectron spectroscopic investigation of nanocrystalline calcium silicate hydrates synthesised by reactive milling, Cem. Concr. Res. 36 (6) (2006) 1023–1031.
[81] J. Li, W. Zhang, K. Xu, P.J.M. Monteiro, Fibrillar calcium silicate hydrate seeds from hydrated tricalcium silicate lower cement demand, Cem. Concr. Res. 137 (2020) 106195.
[82] B. Walkley, J. Provis, Solid-state nuclear magnetic resonance spectroscopy of cements, Mater. Today Adv. 1 (2019) 100007.
[83] I.G. Richardson, Model structures for C-(A)-SH (I), Acta Crystallogr. Sect. B: Struct. Sci. Cryst. Eng. Mater. 70 (6) (2014) 903–923.